JOURNAL OF MATERIALS SCIENCE 37 (2002) 233–248

Hydrocode and microstructural analysis of explosively formed penetrators

S. PAPPU, L. E. MURR
Department of Metallurgical and Materials Engineering and Materials Research Institute, The University of Texas at El Paso, El Paso TX 79968, USA
E-mail: fekberg@utep.edu

A comparison of residual microstructural features in tantalum, iron, and copper explosively-formed projectiles (EFP's) utilizing optical and transmission electron microscopy (TEM) was undertaken and these observations correlated with corresponding microhardness maps measured on the recovered EFP half sections. These microstructural comparisons and residual microhardness maps were then used to validate AUTODYN-2D hydrocode simulations of residual yield stress profiles and the geometrical parameters measured from the recovered EFP's. Both Johnson-Cook and Zerilli-Armstrong constitutive relations were applied and compared in these simulations which also examined the initiation parameters on EFP evolution. Calculated plastic strain and temperature contour plots were also correlated with observed microstructures and the microhardness maps.

1. Introduction

An explosively formed projectile (EFP) liner undergoes extreme, yet controlled, plastic deformation without breaking. This makes designing an optimal EFP a very complicated task. The EFP formation process involves essentially superplastic strains up to 300%, at strain rates of the order of 10^4 s^{-1}, with a resulting adiabatic temperature rise of up to 1000 K or more. Such superplastic-like behavior cannot be explained by conventional theories that only use dislocation generation and arrangements to accommodate strain. A simple schematic of the EFP formation process is shown in Fig. 1.

The dynamic interactions between the explosive products, base plate, confinement and liner present a challenging problem [1]. Although the initial shock-wave-liner interaction may be considered to be approximately planar, there are several basic parameters in the warhead configuration that affect the projectile shape and performance. These can broadly be classified as geometrical factors and material factors.

Liner contours, physical dimensions of the explosive charge, confinement configurations, and explosive initiation technique are some of the geometrical factors of interest. Axial thickness, the presence of taper (or lack thereof), and angle of the liner (α in Fig. 1) have been observed to affect the shape of the EFP. Johnson [2] studied the effect of a tapered liner where the thickness varied linearly from $0.9t_0$ at the top to $1.1t_0$ at the bottom; where t_0 is the thickness of a uniform thickness liner having the same mass. He found that this condition resulted in a significant rotational velocity. Weickert [3] and Hallquist [4] found that different liner geometries resulted in forward-folding, rear-folding or W-fold EFP devices. Hermann *et al.* [5] also studied the effect of various liner designs in addition to the effect of a confined charge.

The charge length is an important design parameter to increase the kinetic energy of the EFP [6, 7]. It was observed that increasing the charge length increases the projectile energy. Blache and Weimann [6] also showed that the contour of the detonation wave has a greater impact on the transfer of energy to the liner than does the charge length. They used devices consisting of a plate with a special mass distribution to achieve the desired detonation wave contours. The length-to-diameter ratio of the explosive charge, L/D, is another important consideration [8]. As L/D is increased, the kinetic energy of the EFP increases until a point of diminishing returns is reached [8].

The EFP case provides confinement for the explosive (Fig. 1). The addition of mass around the explosive and liner increases the duration of the explosive impulse and hence the total energy delivered to the liner [8]. Yiu studied the effects of asymmetric confinement on EFP formation [8, 9]. The explosive and liner were surrounded by a two-piece case made of 180° of steel and 180° of epoxy. A severely distorted EFP was produced due to the unbalanced explosive impulse caused by the uneven venting of explosive products. It has also been shown that a thicker case promotes a more solid, compact projectile than does a thinner case [8]. In another study [10], it was reported that increasing the case thickness of a small cylindrical segment near the rim of the liner resulted in the break-up of the projectile. Weimann [11] and Weickert and Gallagher [12, 13] have shown that there is a pronounced effect on the velocity and shape of an EFP based on the amount of additional

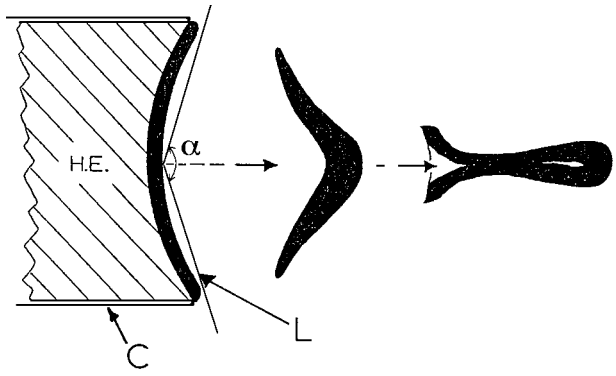

Figure 1 In-flight, self-formation of an EFP from a detonated liner marked L. The high explosive is marked H.E. which is contained within a case, C, usually made of steel of varying thicknesses which actually play a role in the self-forming process. The liner angle is shown by α.

confinement provided by placing a ring, or sleeve over the case. They found that a radially symmetric distribution of confinement produces fins in the EFP.

Johnson [2] studied the effect of an off-center detonation where the explosive was detonated at a point 1.06 cm above the centerline. Initially, the upper portion of the liner experiences the shock so that the liner has a clockwise rotational velocity. As this part of the liner moves away from the explosive at a faster rate, the pressure on it is decreased relative to the bottom portion, which now experiences the shock, thereby causing a final counterclockwise rotation.

The material factors include the structure and properties of the liner, casing and explosive, and the processing conditions during the manufacturing of the liner blanks.

The properties of the liner that are important in the context of the dynamic EFP formation process and its eventual effectiveness as a penetrator are high density, high ductility, high strength and a high enough melting temperature to prevent melting in the liner due to adiabatic heating. Ta, Cu, Fe, and Ta-W alloys show a good combination of these properties and are the most common materials of choice. Grain size and hardness of the starting material are also important, but no systematic studies have been carried out to assess their effect.

The casing is typically made of steel because of its low cost, high strength, and density. However, most any materials can be used, as long as the mass is sufficient to provide the necessary confinement [8].

The explosive properties of importance are the explosive density, detonation velocity and the explosive energy. Johnson [2] studied the effect of a variable density explosive on the EFP formation. As expected, the denser part of the explosive charge imparted a higher velocity to the liner resulting in an angular velocity.

Faccini and Woodbury [14] studied the reasons for undesirable variance in the performance of Ta EFPs. They investigated the effect of initial anneal, amount of pre-strain prior to the initial anneal, amount of Ta removed from the diameter prior to forging, forging temperature, forging rate, liner annealing temperature, and material lot using 14 quality characteristics. They found that different sets of factors affected different quality characteristics but the material lot, forging temperature and amount of pre-strain were major factors affecting the greatest number of quality characteristics.

It is therefore quite apparent that there are a lot of factors that affect the shape and performance of an EFP. Various investigators have studied the effects of different factors, and their efforts have resulted in much improved warheads over the years. The EFP system, however, is far from understood completely and there remain many issues that need to be investigated further. A detailed, systematic microstructural study of various EFP systems is necessary to gaining such an understanding.

The high cost of conducting experiments and the rapid advancements in computer technologies is driving more and more researchers to carry out simulations using hydrocodes in order to design and improve the performance of the EFPs and, of course, many other materials, materials issues, and materials systems. In order for the hydrocodes to have a good predictive capability, they need to be validated against experimental data. Most such validations have focused on matching the experimental shape of the EFP with the predicted shape. Microstructure-based hydrocode validations have not been carried out, mainly due to the sheer number of factors involved [15]. Nonetheless, it is absolutely important that such a validation be carried out in order to have greater confidence in computer-based design. Pappu and Murr [16, 17] have shown the importance of such microstructure-based validations and Quinones [18] has carried out such validations on hypervelocity impact craters.

Traditionally, hydrocode development has depended upon having equations of state (EOS) and constitutive relationships based on shock wave and high-rate experiments [19]. An equation of state relates the density (or volume) and internal energy (or temperature) of the material with pressure, and a constitutive relation describes the particular nature of the material by relating the stress in the material with the amount of distortion (strain) required to produce this stress [20]. The constitutive relations have been improved over the years but these models are only a numeric fit to test data [21, 22]. Zerilli and Armstrong [21] recognized the importance of crystal structure on the dislocation behavior and developed constitutive relations for BCC and FCC structures. They have also considered twinning and dislocation aspects of shock-wave loading [23, 24]. Still, a need remains to develop a more complete constitutive model that incorporates shock-induced effects and the role of dynamic recrystallization (DRX) as a large strain mechanism, especially since the EFP liners are transformed to a new starting state (after shock loading) for the high-rate flow problem that follows [19]. Andrade *et al*. [25] incorporated a reducer function in the Johnson-Cook formulation to represent DRX in work-hardened and shock-hardened copper. Murphy and Lassila [26] tried to incorporate shock effects in a Cu EFP but their model could not predict the EFP shape as well as the Zerilli-Armstrong model. Their ongoing studies are aimed at addressing this issue.

Despite these deficiencies, computational simulations are increasingly being used to design and control experiments, optimize geometries, estimate loading histories, and aid in the interpretation of results, even for

investigations aimed at improving constitutive descriptions [19]. This seemingly ironic trend (using experiments to improve hydrocodes and vice-versa) points to the degree of sophistication that exists in the field, and demonstrates a valuable interplay between the materials and computational disciplines [19].

As noted above, in spite of significant advances made in incorporating materials issues in constitutive relations, much remains to be understood about the basic deformation mechanisms operating at high strain rates, e.g., DRX. Practically nothing has been done to address this issue by way of material microstructural analysis. A group of researchers at the University of Waterloo and the Defence Research Establishment, Suffield in Canada made an effort to study and correlate hydrocode predictions with observed microstructures in "soft" recovered Ta, Armco Fe and Cu EFPs [27–29]. However, no detailed TEM analyses were done. Murr and coworkers [30–34] recently carried out a detailed, TEM microstructural analysis on Ta EFPs.

Ta has a very high melting temperature, T_m (~3020°C) and it is unlikely that adiabatic temperature rise is enough to cause recrystallization in the classical sense. Fe, like Ta, has a BCC structure but approximately half the T_m (1539°C). Cu, on the other hand, has a T_m closer to that of Fe (1083°C) but has a FCC structure. Consequently, Cu has different slip and deformation characteristics than Fe and Ta.

A detailed, comparative microstructural analysis was carried out on Ta, Armco Fe, and OFHC Cu EFPs in this study, and the microstructural issues utilized in validating the AUTODYN-2D hydrocode along with comparative geometrical parameters measured for soft-recovered EFP's. In addition, comparisons were made for computations involving both the Johnson-Cook and the Zerilli-Armstrong constitutive relationships.

2. Experimental details

The Ta EFP was made from a pure Ta rolled plate. The EFP, moving at 2.25 km/s, was caught without causing further deformation using a soft-recovery set-up. The Armco Fe EFP liner was machined from a 25 mm hot rolled, domed plate purchased from ARMCO GmBH. The liner, 100 mm in diameter, was given a stress relieving anneal prior to explosive filling. The case was constructed of mild steel with a wall thickness of 1 mm. A 6 mm thick mild steel slotted ring with equally spaced slots (5 mm × 10 mm) machined vertically along the outside surface (i.e., parallel to the flight direction) was glued to the case, flush with the front of the case. The base, made of 6061 Al, was also glued onto the rear of the case. A cast-loaded 60/40 Composition B (59.5% RDX, 39.5% TNT, 1% wax) high explosive was used, which was initiated by a pressed A-5 explosive precision booster and an RP-83 detonator [11,35]. The Cu EFP was obtained from a dish-shaped oxygen-free high-conductivity (OFHC) copper liner backed by Octol (HMX-TNT) high explosive [29]. The EFP fractured during the test and recovery.

The EFPs were sliced in half along their longitudinal axes. Fig. 2 shows the soft-recovered and sectioned

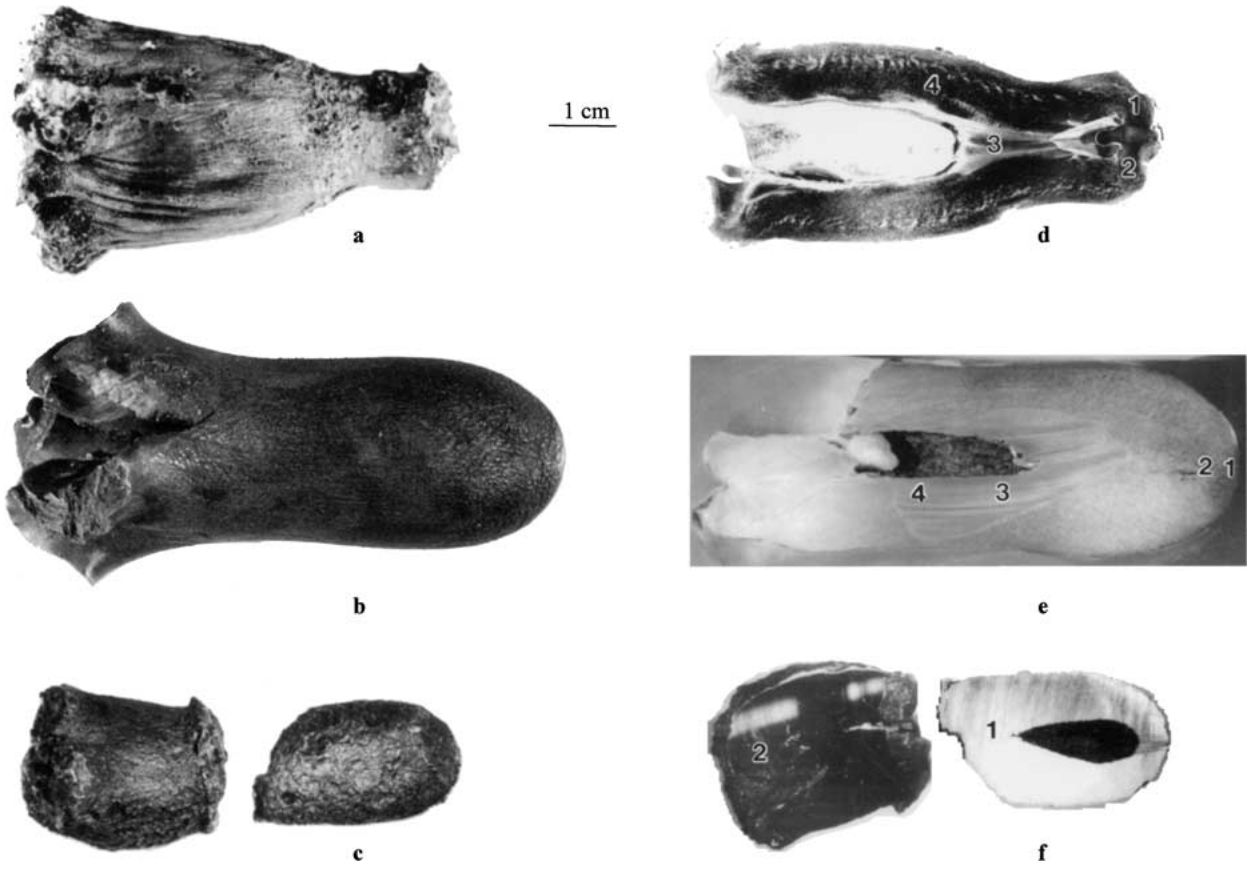

Figure 2 Soft-recovered EFP projectiles and their corresponding, longitudinally sliced half-sections. Ta (a) and (d); Fe (b) and (e); Cu (c) and (f) – respectively. The Cu EFP in (c) and (f) was broken during the recovery process.

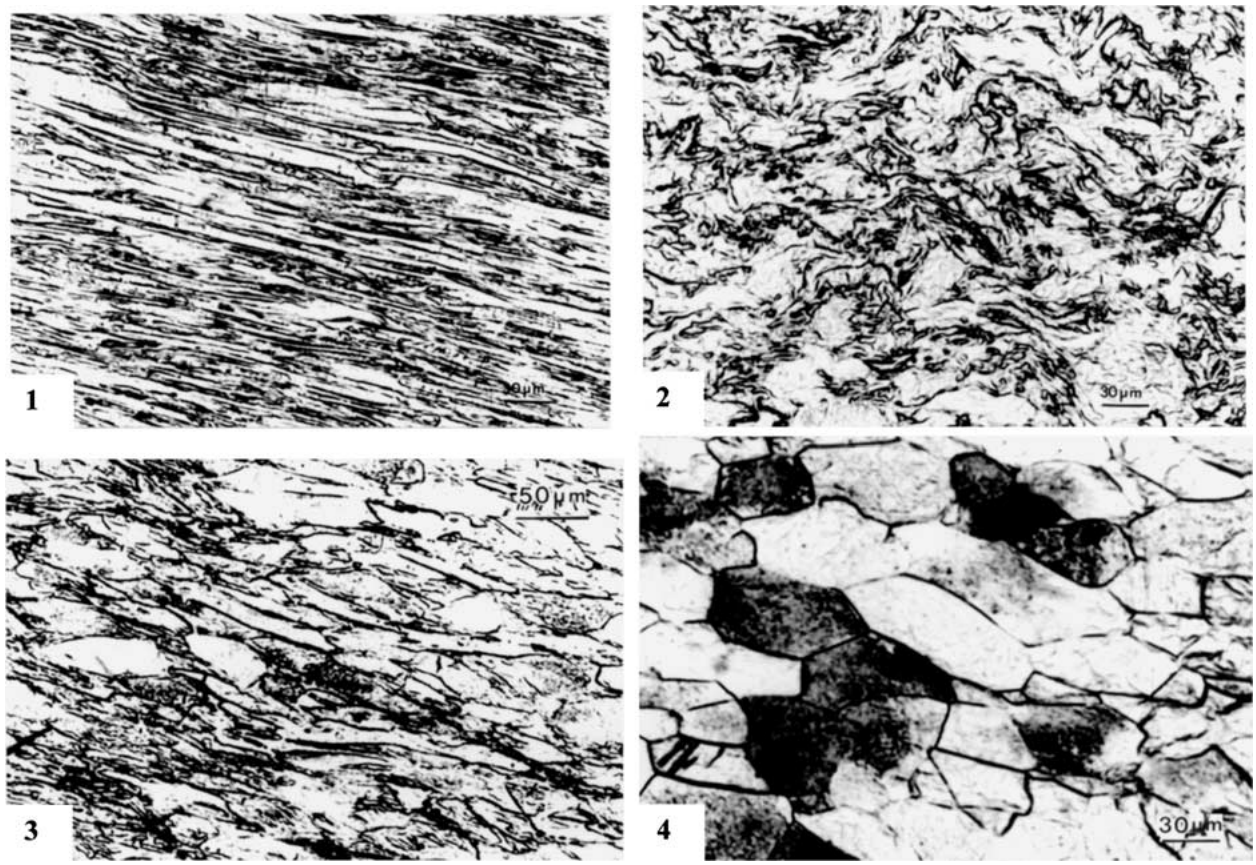

Figure 3 Optical metallographic images of microstructures characteristic of the zones numbered correspondingly in the Ta half section in Fig. 2d.

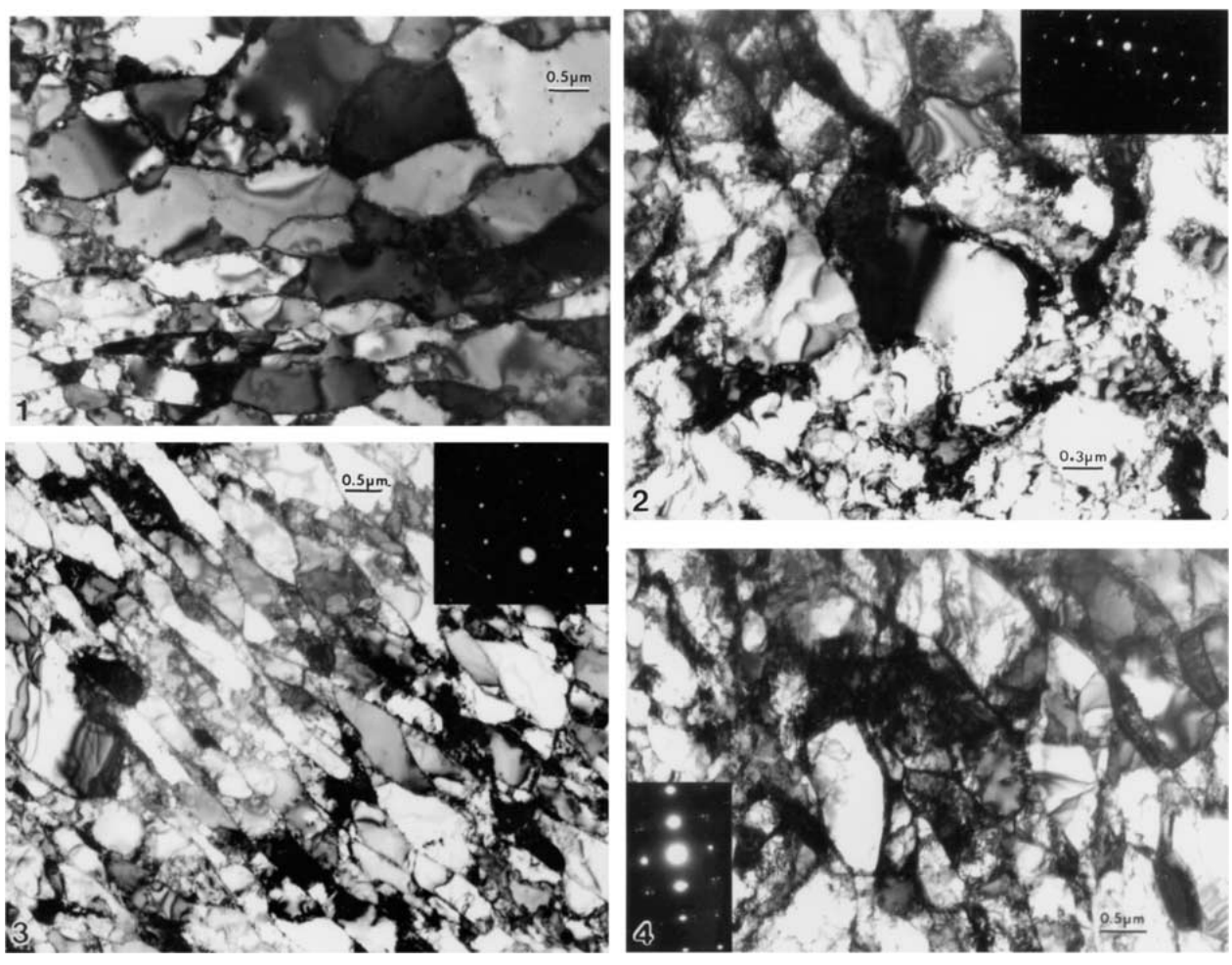

Figure 4 TEM bright-field images of microstructures corresponding to the regions indicated in Fig. 3 and Fig. 2d.

EFPs. Mounted half-sections of the EFPs were ground and polished using standard optical metallographic practices. Fine polishing was done using 1 _m and 0.3 _m alumina suspensions to obtain mirror finish. In the case of Cu, colloidal silica (0.04 _m) was used following polishing by alumina suspensions. Etching was done using the following solutions:

(i) Ta: 1 part (by volume) HNO_3, 2 parts HCl and 4 parts HF were individually cooled to 0°C (in ice). HNO_3 and HCl were then mixed and this solution was again cooled to 0°C. Finally, HF was added and the resulting solution again cooled to 0°C before etching.

(ii) Fe: 2% Nital was used for etching at room temperature.

(iii) Cu: Two different etchants were used with similar results. (a) 2 g $K_2Cr_2O_7$, 5 ml H_2SO_4 and 4 ml saturated NaCl in 100 ml H_2O. (b) 40% HNO_3 in H_2O.

Following optical microscopy, microindentation hardness tests were performed on the longitudinal half-sections. Loads of 100 gf (for 5 s), 200 gf (for 10 s), and 50 gf (for 10 s) were applied for Ta, Fe, and Cu, respectively. Microhardness maps were then generated showing zones of varying microhardness recorded as Vickers microhardness (VHN). These were then used in the validation of the AUTODYN-2D hydrocode, utilizing the following correlation between hardness (VHN) and, the engineering yield stress σ_{ys}:

$$\sigma_{ys} \approx \text{VHN}/3(1\ \text{VHN} = 10^{-2}\,\text{GPa});$$

since the hydrocode simulates residual yield stress maps rather than hardness maps.

Thin longitudinal slices were sectioned from the EFP samples following the microindentation hardness testing. These samples were then ground to approximately 150–200 μm thicknesses. 3 mm discs were then punched out from areas showing marked differences in the microstructure and microhardness values. These discs were then jet polished in a Struers Tenupol-3 dual-jet polisher until a hole was formed. The solutions and thinning conditions for the three different materials are as follows:

(i) Ta: 750 ml methanol was added to 150 ml glycerol and the solution cooled to approximately −20°C. 135 ml sulfuric acid was then slowly added with extreme caution and the resulting solution cooled to about −10°C. 75 ml hydrofluoric acid and 350 ml ethanol were then added to this solution, which was then heated to about 8–10°C for jet thinning. The voltage was gradually decreased from 12 V to 8 V during the preparation of each sample. A flow rate of 2 (on a scale of 10) was used, and photosensitivity was kept at 5 (also on a scale of 10).

(ii) Fe: A solution containing 200 ml HCl and 1300 ml methanol was used at −20°C and 25 V.

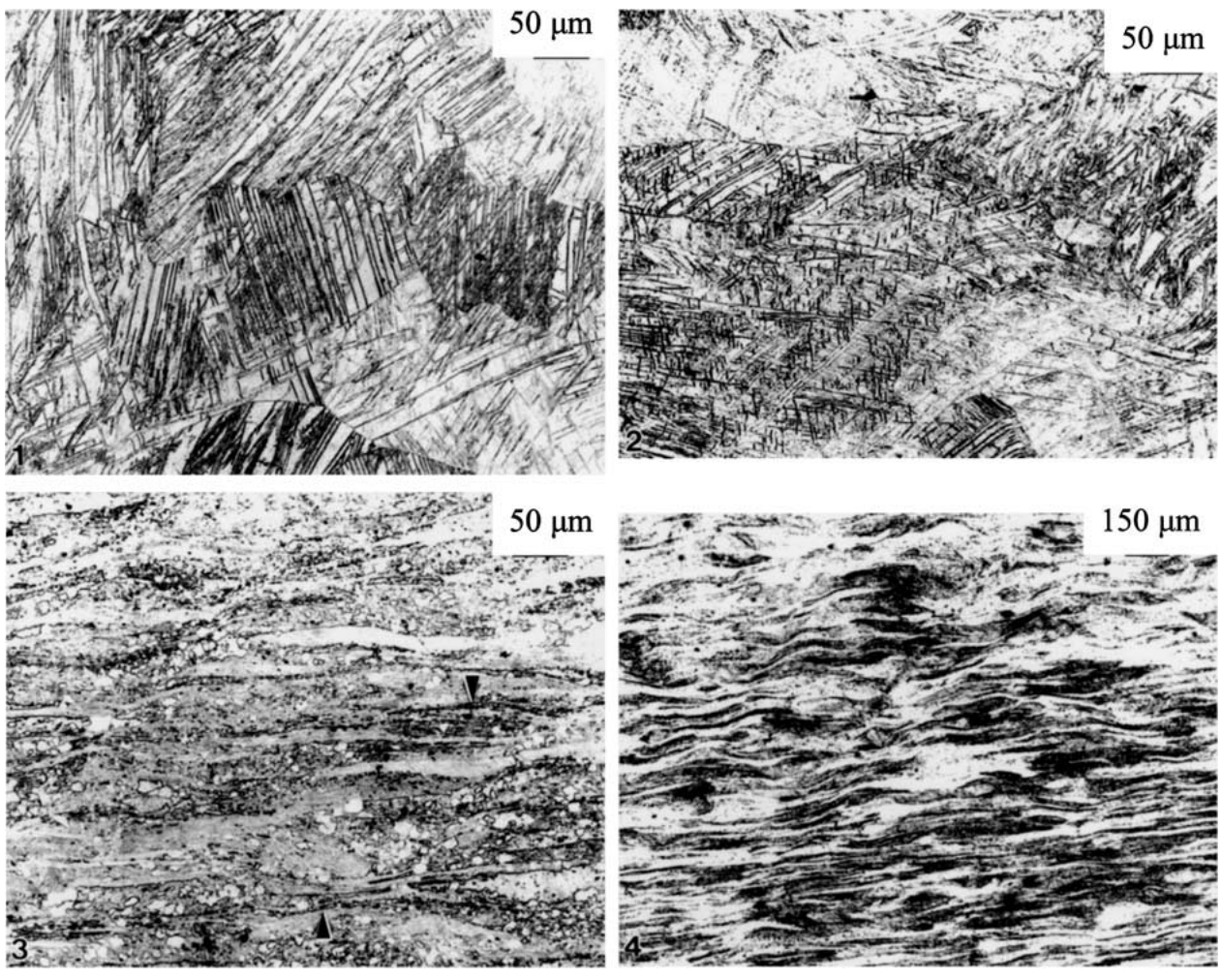

Figure 5 Optical metallogrpahic images of microstructures characteristic of the zones numbered correspondingly in the Fe half section in Fig. 2e.

(iii) Cu: Two different solutions were tried, with similar results. The first solution consisted of 1300 ml methanol, 100 ml propanol, 200 ml nitric acid and 100 ml phosphoric acid. Thinning was done at 9 V and −5°C at a flow rate of 1. The second solution was prepared as follows: 7.5 g urea was dissolved in 825 ml distilled water. This solution was cooled to 0°C before adding 375 ml ethanol and 75 ml propanol. 300 ml phosphoric acid was added after cooling down the solution to 0°C. Thinning was done at 8–10 V and 10°C. A high flow rate of 8 was employed till a dimple formed on the specimen following which the flow rate was reduced to 2 and the thinning continued till a hole was made.

TEM studies were carried out in a Hitachi H-8000 analytical transmission electron microscope (TEM) equipped with a goniometer tilt stage, and operated at 200 kV accelerating potential in the conventional TEM mode.

Computer simulations were performed using the AUTODYN-2D software program. Effective (computed) plastic strain, temperature and yield stress profiles were generated that were correlated with the microstructural observations and the measured hardness values. Simulated EFP shapes were also correlated with shape (geometrical) features measured directly from the recovered, sectioned components shown in Fig. 2.

3. Results and discussion

Fig. 3 shows Ta EFP optical micrographs from various zones marked 1–4 in Fig. 2d. The grain structure varies from heavily deformed, elongated grains in the head section to wavy grains in the mid-section, to lightly deformed and fairly equiaxed grains in the tail region.

The corresponding TEM images in Fig. 4 show a mixture of dislocation cells and subgrains with a range of misorientations as seen in the selected-area electron diffraction (SAED) pattern inserts. These

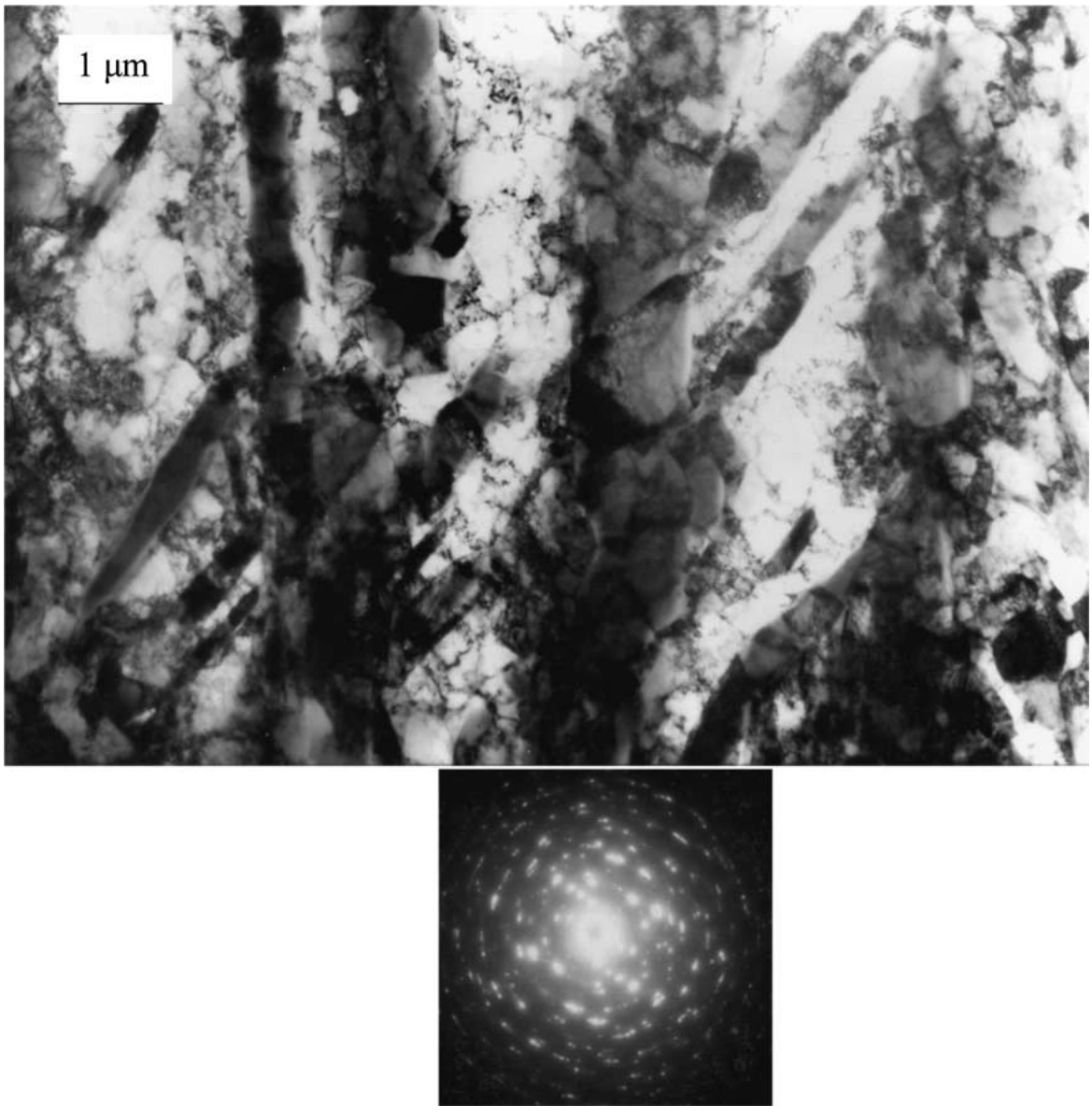

Figure 6 TEM bright-field image showing a mixture of twin segments, recovery microstructures, and very small dynamically recrystallized (DRX) grains. Although difficult to differentiate in the image, the included SAED pattern shows a variety of misorientation angles and other reflections characteristic of all of these features.

microstructures are representative of dynamic recovery (DRV), which appears to be the predominant mechanism in the Ta EFP formation process.

Microstructural variation in the Fe EFP is illustrated in the optical micrographs in Fig. 5. Extensive Neumann banding and the association of fragmenting Neumann bands with dynamically recrystallized grains and correspondingly with shear bands appears to be the predominant mechanism in the Fe EFP formation process. Pappu and Murr [36] have recently shown the correspondence of Neumann bands with deformation twins in the iron EFP by observing systematic $\langle hkl \rangle/3$ twin reflections in SAED patterns and utilizing these reflections to form dark-field images showing the twins. Numerous examples involving bright and dark-field TEM combined with SAED patterns indicated, as others have previously noted, that the Neumann bands shown in Fig. 5 were deformation twins. The TEM image in Fig. 6 shows a mixture of twins, DRV and DRX structures as evidenced by a range of misorientations and the polycrystalline nature of the SAED pattern.

Representative optical and TEM micrographs in the Cu EFP are shown in Fig. 7. Small, equiaxed grains, shear bands containing tiny, recrystallized grains, dislocation cells and annealing twins mark the microstructure all along the EFP half-section. That is, the Cu EFP undergoes complete recrystallization.

The microstructural analysis showed that Ta is characterized by DRV, Cu by complete recrystallization (possibly a combination of DRX and static recrystallization) and Fe by extensive twinning, which is associated with DRX (as a precursor), and the corresponding shear bands. Tang *et al*. [29] observed deformation twins in a shear band that was not fully formed in a Cu EFP, although TEM evidence was not provided. Pappu *et al*. [37] observed a similar relationship between twinning and DRX in W long-rod ballistic projectiles that were fired into RHA targets. RHA denotes rolled homogeneous armor which for standard U.S. military armor is rolled medium carbon steel plate (MIL-A-12560, class 3 steel).

Computer simulations were performed to validate the hydrocode utilizing geometrical as well as microstructural issues. Table I shows the input material parameters for the base and the case for Ta and Fe EFP simulations. Table II shows these parameters for the Cu EFP simulation. The input parameters for explosives used in the simulations are shown in Table III.

The correspondence of experimentally measured microhardness profiles for the three EFPs with the computed yield stress profiles is shown in Fig. 8. The hardness in the Ta EFP varies from 144 VHN to 200 VHN. The yield stress varies from approximately 0.72 GPa to 0.92 GPa, which corresponds to

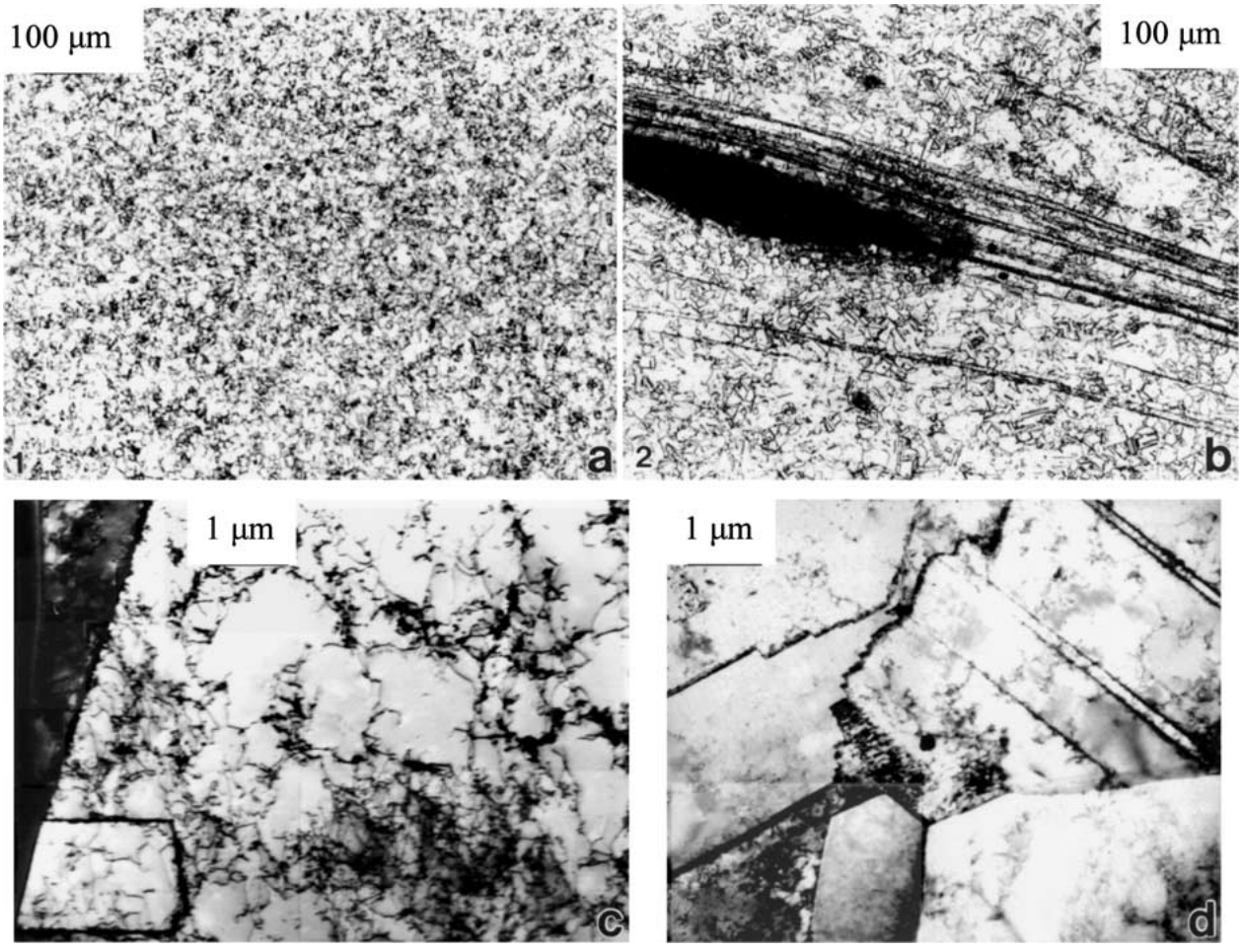

Figure 7 Optical micrographs ((a) and (b)) and corresponding TEM bright-field images ((c) and (d)) characteristic of the Cu EFP microstructures. The numbers in (a) and (b) correpsond to the half-section locations shown in Fig. 2f. The linear features in (d) are annealing twins or recrystallization twins.

TABLE I Material parameters for base and case for Ta and Armco Fe EFP simulations

Parameter	1006 Steel (Case for Ta and Fe)	2024-T351 Al (Base for Ta and Fe)
Equation of state	Shock	Shock
Reference density (g/cm^3)	7.89600E + 00	2.78500E + 00
Gruneisen coefficient	2.17000E + 00	2.00000E + 00
Parameter C_1 (m/s)	4.56900E + 03	5.32800E + 03
Parameter S_1	1.49000E + 00	1.33800E + 00
Parameter quad. S_2 (s/m)	0.00000E + 00	0.00000E + 00
Relative volume, V_E	0.00000E + 00	0.00000E + 00
Relative volume, V_B	0.00000E + 00	0.00000E + 00
Parameter C_2 (m/s)	0.00000E + 00	0.00000E + 00
Parameter S_2	0.00000E + 00	0.00000E + 00
Reference temperature (K)	3.00000E + 02	3.00000E + 02
Specific heat (C.V.) (J/kg K)	4.52000E + 02	8.75000E + 02
Strength model	Johnson-Cook	Johnson-Cook
Shear modulus (kPa)	8.18000E + 07	2.76000E + 07
Yield stress (kPa)	3.50000E + 05	2.65000E + 05
Hardening constant (kPa)	2.75000E + 05	4.26000E + 05
Hardening exponent	3.60000E − 01	3.40000E − 01
Strain rate constant	2.20000E − 02	1.50000E − 02
Thermal softening exponent	1.00000E + 00	1.00000E + 00
Melting temperature (K)	1.81100E + 03	7.75000E + 02
Failure model	None	None
Erosion model	None	None

TABLE II Material parameters for base and case for OFHC Cu EFP simulation

Parameter	1006 Steel (Case for Cu)	6061-T6 Al (Base for Cu)
Equation of state	Linear	Shock
Reference density (g/cm^3)	7.89600E + 00	2.70300E + 00
Bulk modulus (kPa)	1.80000E + 08	–
Gruneisen coefficient	–	1.97000E + 00
Parameter C_1 (m/s)	–	5.24000E + 03
Parameter S_1	–	1.40000E + 00
Parameter quad. S_2 (s/m)	–	0.00000E + 00
Relative volume, V_E	–	0.00000E + 00
Relative volume, V_B	–	0.00000E + 00
Parameter C_2 (m/s)	–	0.00000E + 00
Parameter S_2	–	0.00000E + 00
Reference temperature (K)	3.00000E + 02	3.00000E + 02
Specific heat (C.V.) (J/kg K)	4.52000E + 02	8.85000E + 02
Strength model	Johnson-Cook	Steinberg-Guinan
Shear modulus (kPa)	8.18000E + 07	2.76000E + 07
Yield stress (kPa)	3.50000E + 05	2.90000E + 05
Hardening constant (kPa)	2.75000E + 05	–
Hardening exponent	3.60000E − 01	–
Strain rate constant	2.20000E − 02	–
Thermal softening exponent	1.00000E + 00	–
Maximum yield stress (kPa)	–	6.80000E + 05
Hardening constant	–	1.25000E + 02
Hardening exponent	–	1.00000E − 01
Derivative, dG/dP	–	1.80000E + 00
Derivative, dG/dT (kPa)	–	−1.70000E + 04
Derivative, dσ_{ys}/dP	–	1.89080E − 02
Melting temperature (K)	1.81100E + 03	9.00000E + 02
Failure model	None	None
Erosion model	None	None

TABLE III Input parameters for explosives used in the simulations

Parameter	Composition B (used for Ta and Fe EFPs)	Octol (used for Cu EFP)
Equation of state	Jones-Wilkins-Lee (JWL) (Explosive)	JWL (Explosive)
Reference density (g/cm^3)	1.71700E + 00	1.82100E + 00
Parameter A (kPa)	5.24230E + 08	7.48600E + 08
Parameter B (kPa)	7.67800E + 06	1.33800E + 07
Parameter R_1	4.20000E + 00	4.50000E + 00
Parameter R_2	1.10000E + 00	1.20000E + 00
Parameter ω	3.40000E − 01	3.80000E − 01
C-J Detonation velocity (m/s)	7.98000E + 03	8.48000E + 03
C-J energy/unit volume (kJ/m^3)	8.50000E + 06	9.60000E + 06
C-J pressure (kPa)	2.95000E + 07	3.42000E + 07
Burn on compression fraction	1.00000E − 01	1.00000E − 01
Pre-burn bulk modulus (kPa)	0.00000E + 00	0.00000E + 00
Adiabatic constant (kPa)	0.00000E + 00	0.00000E + 00
Strength model	None (Hydro)	None (Hydro)
Failure model	None	None
Erosion model	None	None

Vickers microindentation hardness values of 216 VHN to 276 VHN. Although the computationally predicted values are higher than the measured values, the range of predicted values (60 VHN) is approximately the same as that of measured values (56 VHN). It should be noted that the predicted values are expected to be somewhat higher because the post-deformation stress-relief due to temperature dissipation is not taken into account by the software. These predicted values are expected to be higher than measured values by a greater degree in Ta than in Fe and Cu due to the much higher temperatures experienced by Ta. In general, the predicted yield stress variation is in fairly good agreement with the hardness variation. There is a small soft zone followed by a harder zone at the tip of the EFP head. The mid-section and isolated pockets along the periphery are the hardest with the tail having slightly lower hardness values.

The microhardness values in the Fe EFP range between 128 VHN and 245 VHN. The yield stress values vary from approximately 0.5 GPa to 1 GPa, which correspond to Vickers microhardness values of 150 VHN to 300 VHN. As with Ta, the predicted values are higher than measured values, but not as much. This is due to much lower temperatures experienced by Fe, which do not lower the stresses following deformation as much as they do in Ta. The hydrocode predicts the general features (which include a harder zone in the head than in the center and the hardest zone in the tail) fairly well although the predicted soft zone in the EFP center is exaggerated.

In accordance with the negligible microstructural variation, the microhardness values are also uniform across the span of the Cu EFP. There is only a minor variation, with the hardness being 69 VHN in the head and 62 VHN in the tail. The yield stress values range approximately between 0.25 GPa and 0.30 GPa, corresponding to hardness values between 75 VHN and 90 VHN; again somewhat higher than the measured values. There is nonetheless, fairly good agreement between the computed and measured values.

Fig. 9 shows the effective plastic strain and temperature profiles in the three EFPs as predicted by the AUTODYN-2D hydrocode. The results in Figs 8 and 9 are summarized in Tables IV through IX, which show the geometrical and microstructure-based validation of the hydrocode. A rigorous geometrical validation of the Cu EFP was not attempted since the actual EFP broke

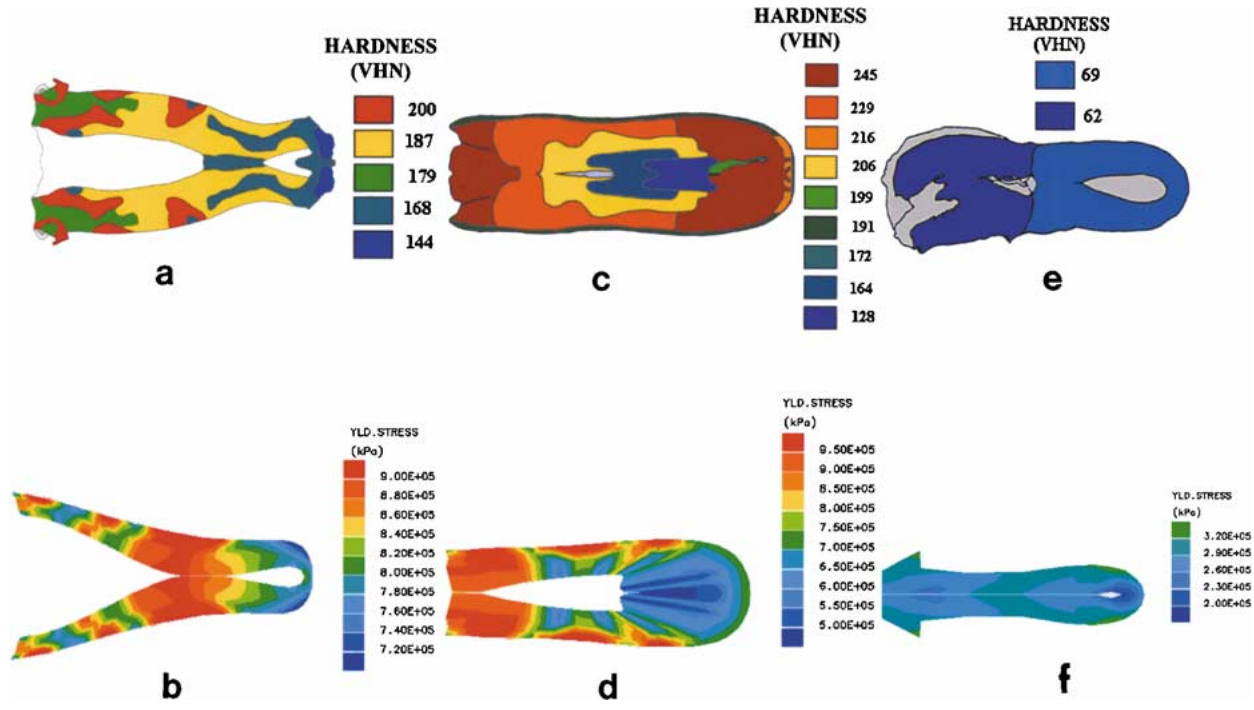

Figure 8 Comparison of experimentally measured, residual Vickers microhardness half-section maps with computed, residual yield stress profiles in simulated sections. Ta: (a) and (b); Fe: (c) and (d); Cu: (e) and (f). Ta and Cu ((b) and (f)) respectively used the Zerilli-Armstrong constitutive model while for Fe in (d) the Johnson-Cook model was employed.

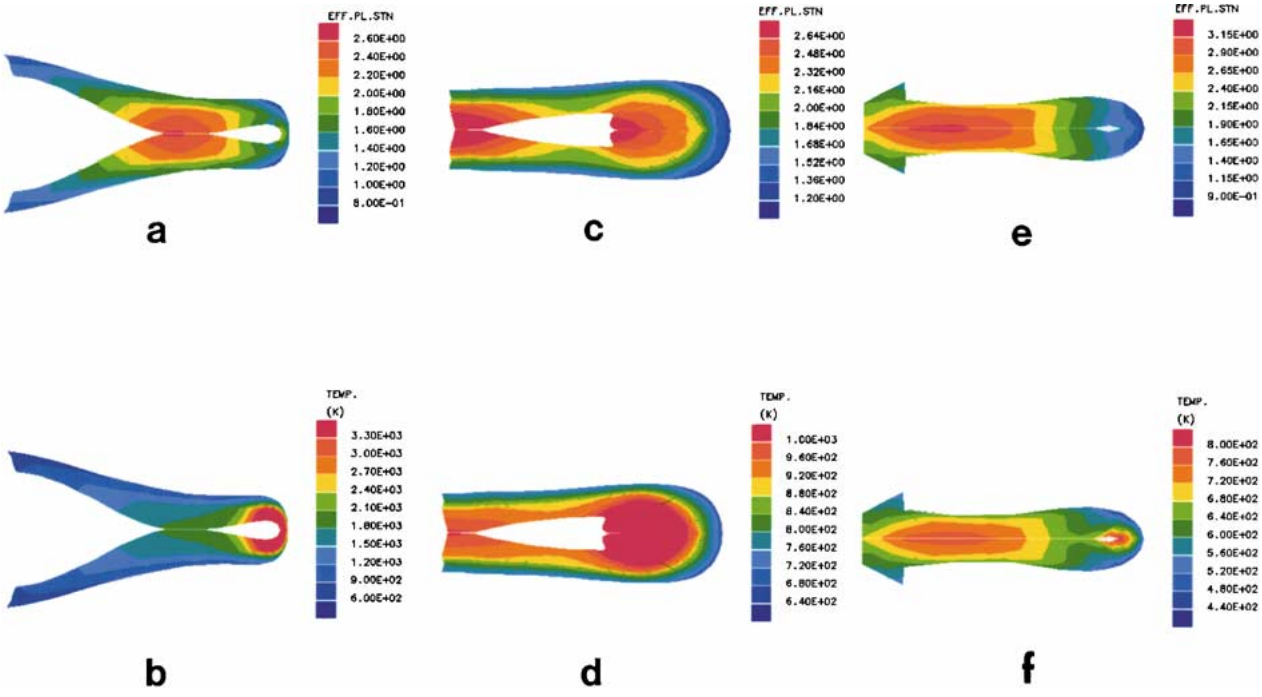

Figure 9 Comparison of computed effective plastic strain and temperature profiles for the three experimental EFP's. Ta: (a) and (b); Fe: (c) and (d); Cu: (e) and (f). Ta and Cu ((b) and (f)) respectively used the Zerilli-Armstrong constitutive model while for Fe in (d) the Johnson-Cook model was employed.

into two pieces. However, the general shape features (such as the internal cavity) are fairly well simulated.

It should be noted that although geometrical, and microstructure and property-based validations were achieved, Fe was better described by the Johnson-Cook strength (constitutive) model, whereas Ta and Cu were better simulated using the Zerilli-Armstrong strength model.

Tables X and XI show the Johnson-Cook and Zerilli-Armstrong parameters for the three EFP liners,

TABLE IV Comparison between actual and simulated geometrical parameters-Ta

Parameter	Experiment	Simulation
Length (cm)	6.87	7.53
Width at head (cm)	2.07	1.87
Width at tail (cm)	3.13	4.13
Maximum void width (cm)	0.63	0.47
Void length (cm)	1.07	1.87
Length of mid-section behind void (cm)	1.30	1.27

TABLE V Correspondence of effective plastic strains, temperatures and hardness values for microstructural features in various Ta EFP regions

Region no.	Effective plastic strain, _	Temperature (K)	Microstructural features		VHN
			Optical	TEM	
1	1.4–1.8	>3300	Fairly equiaxed grains	Well-developed subgrains and dislocation cells	167
2	1.8–2.0	> 3300	Highly deformed and elongated grains	Well-developed subgrains and dislocation cells	167
3	2.4–3.0	1800–2100	Highly deformed and elongated grains	Well-developed subgrains and dislocation cells	170
4	1.6–2.2	1200–1500	Deformed, wavy grains	Well-developed subgrains and dislocation cells	187
5	0.8–1.2	600–900	Lightly deformed, elongated grains	Elongated dislocation cells	179
6	1.2–1.4	900–1200	Fairly equiaxed grains	Well-developed subgrains	199

TABLE VI Comparison between actual and simulated geometrical parameters—Fe

Parameter	Experiment	Simulation
Length (cm)	8.00	7.67
Maximum width at head (cm)	2.80	2.65
Tail width (cm)	2.28	2.10
Length/Head width ratio	2.86	2.89
Tip to void distance (cm)	3.30	3.26
Maximum void width (cm)	0.70	0.85

respectively. The input yield stress values were increased from the material library values included in the software to account for the initial shock-induced hardening of the liners prior to the in-flight deformation. For reference, the Zerilli-Armstrong and Johnson-Cook constitutive equations are given below:

Johnson-Cook:

$$\sigma_{\text{eff}} = \left[A + B\varepsilon_{\text{p}}^{n}\right]\left[1 + C\log\varepsilon_{\text{p}}^{\prime *}\right]\left[1 - T_{\text{H}}^{\text{m}}\right] \quad (1)$$

Zerilli-Armstrong (FCC):

$$\sigma = \sigma_0 + C_2\varepsilon^{1/2}\exp[-C_3T + C_4T\log\varepsilon'] \quad (2)$$

Zerilli-Armstrong (BCC):

$$\sigma = \sigma_0 + C_1\exp[-C_3T + C_4T\log\varepsilon'] + C_5\varepsilon^{n} \quad (3)$$

Fig. 10 shows the resultant EFP shape and yield stress profiles due to the different strength models. It can be seen that both the Johnson-Cook and Zerilli-Armstrong models give fairly similar EFP shapes, although the heads show some obvious differences. These minor differences can be fixed by "tuning" the input parameters. However, significant differences exist in the end-results. Whereas the Zerilli-Armstrong model predicts the head to be softer than the back sections, the Johnson-Cook model predicts a small region in the head section that is harder (higher yield stress) than in the region behind it. Also, the range of yield stress values (difference between the maximum and minimum values) is much larger in the Johnson-Cook formulation than in the Zerilli-Armstrong formulation.

In the case of Cu, both the Johnson-Cook and Zerilli-Armstrong models predict similar shapes and properties. On comparing the Johnson-Cook model predictions of yield stress for Ta, Fe and Cu EFPs, it can be observed that the range is maximum for Ta and minimum for Cu. This can be explained by considering the thermal softening term of the Johnson-Cook equation, viz., $\{1 - [(T - T_{\text{room}})/(T_{\text{melt}} - T_{\text{room}})]^m\}$. Ta has the highest T_{melt} (3293 K) and lowest thermal softening exponent ($m = 0.44$), whereas Cu has the lowest T_{melt} (1356 K) and highest m (1.09). Also, the temperature rise, $(T - T_{\text{room}})$ is maximum for Ta and minimum for Cu. Due to these reasons, the variation in thermal softening term is smallest in Cu and highest in Ta, resulting in the minimum yield stress variation in Cu and maximum in Ta.

The reversal of properties in the head and back sections of the EFP can have important consequences in the predicted performance of the EFP. It is, therefore, extremely important to carry out not only shape-based validations of the hydrocodes but also structure/property-based validations. Since properties are intimately

TABLE VIII Comparison between actual and simulated geometrical parameters—Cu

Parameter	Experiment	Simulation
Length (cm)	6.60	9.80
Maximum width at head (cm)	2.03	2.30
Tail width (cm)	1.90	1.90
Tip to void distance (cm)	0.47	1.00
Void length (cm)	1.89	0.80

TABLE VII Correspondence of effective plastic strains, temperatures and hardness values for microstructural features in various Fe EFP regions

Region no.	Effective plastic strain, γ	Temperature (K)	Microstructural features	VHN
1	1.2–1.5	680–760	Neumann bands (twins)	216
2	2.5–3.0	>1000	DRX grains and grain growth	128
3	1.4–1.7	680–760	Deforming twins; recovery and recrystallization structures	191
4	2.3–2.5	960–1000	Fragmenting twins, DRX grains and shear bands	164
5	1.7–2.0	720–800	Deforming twins	191
6	2.6–3.0	960–1000	Deforming grains containing twins	245

TABLE IX Correspondence of effective plastic strains, temperatures and hardness values for microstructural features in various Cu EFP regions

Region no.	Effective plastic strain, γ	Temperature (K)	Microstructural features	VHN
1	1.15–1.40	520–560	Recrystallized grains, dislocation cells, annealing twins	69
2	1.40–1.65	720–800	-same-	69
3	1.90–2.15	560–640	-same-	69
4	2.40–2.65	680–720	-same-	69
5	1.90–2.15	560–600	-same-	62
6	2.15–2.40	600–640	-same-	62

related to the structure of the material, any such validations can be done satisfactorily only by studying the internal structure or microstructure.

As mentioned earlier, the constitutive parameters are generally a numerical fit to a particular set of data. Constitutive parameters obtained from validating experiments need not necessarily apply to the experimental conditions under study. Table XII shows Zerilli-Armstrong constitutive parameters from two different sources. The resultant simulated EFPs are shown in Fig. 11.

The effects of various geometrical factors on the final EFP shape are shown in Fig. 12. On initiating

TABLE X Johnson-Cook material parameters for EFP liners

Parameter	Tantalum	Armco iron	OFHC copper
Equation of state	Linear	Linear	Linear
Reference density (g/cm^3)	1.66900E + 01	7.89000E + 00	8.96000E + 00
Bulk modulus (kPa)	1.50000E + 08	1.64000E + 08	1.29000E + 08
Reference temperature (K)	3.00000E + 02	3.00000E + 00	3.00000E + 02
Specific heat (C.V.) (J/kg K)	1.35000E + 02	4.52000E + 02	3.83000E + 02
Strength model	Johnson-Cook	Johnson-Cook	Johnson-Cook
Shear modulus (kPa)	6.90000E + 07	8.00000E + 07	4.60000E + 07
Yield stress (A) (kPa)	8.00000E + 05	1.00000E + 06	1.00000E + 05
Hardening constant (B) (kPa)	5.50000E + 05	3.80000E + 05	2.92000E + 05
Hardening exponent (n)	4.00000E − 01	3.10000E − 01	3.10000E − 01
Strain rate constant (C)	5.75000E − 02	6.00000E − 02	2.50000E − 02
Thermal softening exponent (m)	4.40000E − 01	5.50000E − 01	1.09000E + 00
Melting temperature (K)	3.29300E + 03	1.81200E + 03	1.35600E + 03
Erosion model	Instantaneous Geometric strain	Instantaneous Geometric strain	Instantaneous Geometric strain
Erosion strain	5.00000E + 00	5.00000E + 00	5.00000E + 00
Failure model	None	None	None

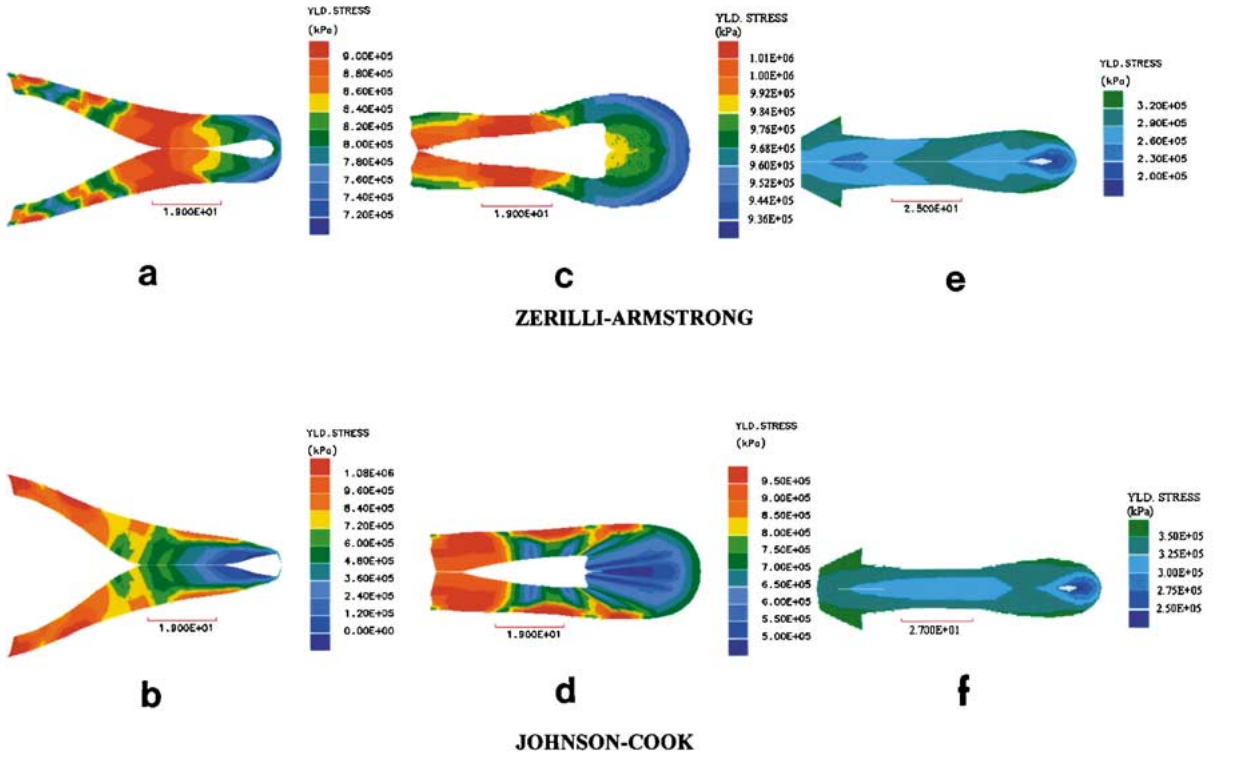

Figure 10 Comparison of residual yield stress profiles computed with Zerilli-Armstrong and Johnson-Cook constitutive relationships, respectively for the experimental EFP materials. Ta: (a) and (b); Fe: (c) and (d); Cu: (e) and (f). Note scale units are in cm.

TABLE XI Zerilli-Armstrong material parameters for EFP liners

Parameter	Tantalum	Armco iron	OFHC copper
Equation of state	Linear	Linear	Linear
Reference density (g/cm^3)	1.66900E + 01	7.89000E + 00	8.96000E + 00
Bulk modulus (kPa)	1.50000E + 08	1.64000E + 08	1.29000E + 08
Reference temperature (K)	3.00000E + 02	3.00000E + 00	3.00000E + 02
Specific heat (C.V.) (J/kg K)	1.35000E + 02	4.52000E + 02	3.83000E + 02
Strength model	Zerilli-Armstrong	Zerilli-Armstrong	Zerilli-Armstrong
Shear modulus (kPa)	6.90000E + 07	8.00000E + 07	4.60000E + 07
Yield stress (kPa)	4.00000E + 05	6.50000E + 05	6.50000E + 04
C_1 (kPa)	1.12500E + 06	1.03300E + 06	0.00000E + 00
C_2 (kPa)	0.00000E + 00	0.00000E + 00	8.90000E + 05
C_3	5.35000E − 03	6.98000E − 03	2.80000E − 03
C_4	3.27000E − 04	4.15000E − 04	1.15000E − 04
C_5 (kPa)	3.10000E + 05	2.66000E + 05	0.00000E + 00
N	4.40000E − 01	2.89000E − 01	0.00000E + 00
Erosion model	Instantaneous Geometric strain	Instantaneous Geometric strain	Instantaneous Geometric strain
Erosion strain	5.00000E + 00	5.00000E + 00	5.00000E + 00
Failure model	None	None	None

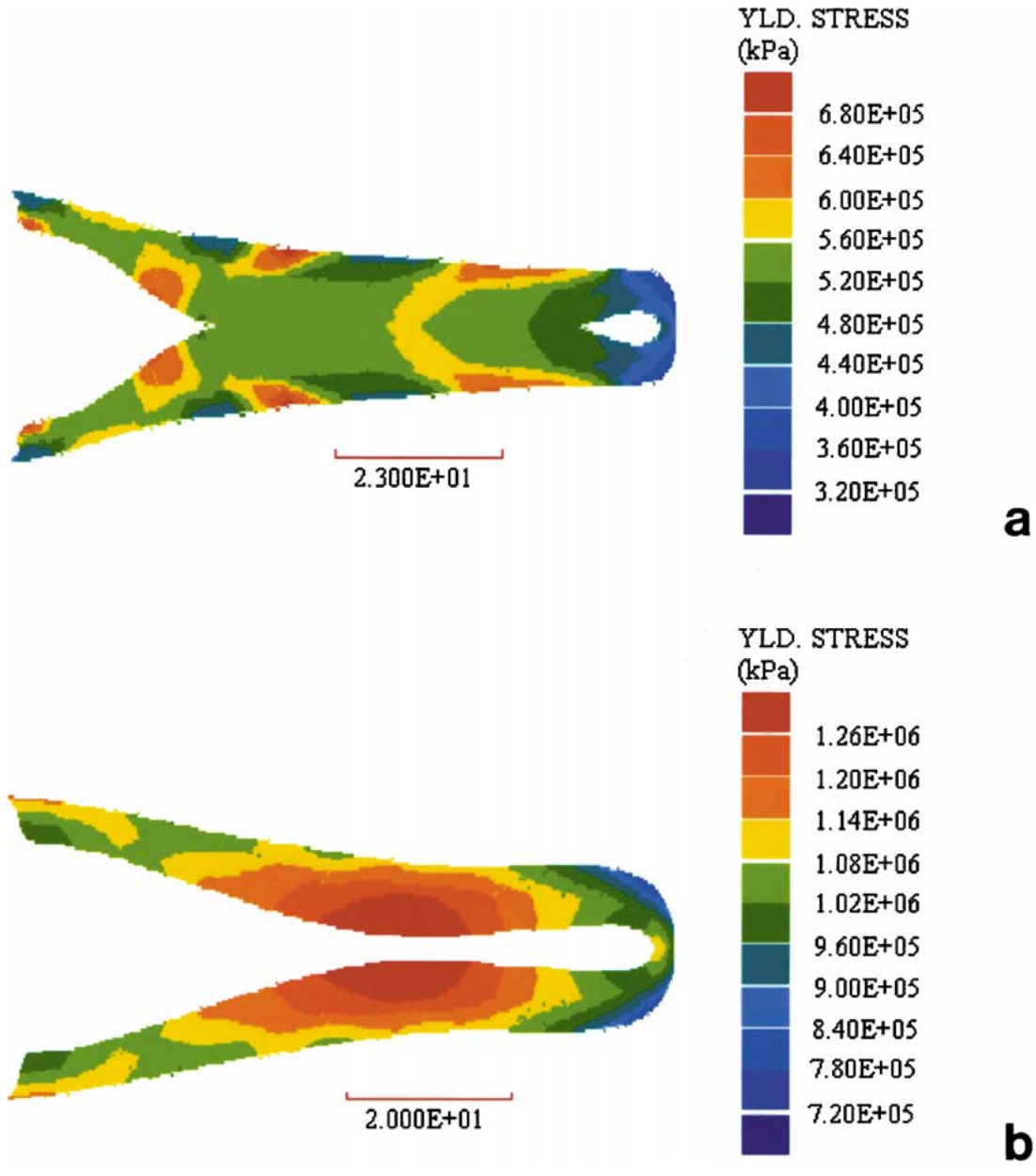

Figure 11 Effect on computed yield stress contours for Ta EFP's of utilizing material parameters from different success for the same strength model (Zerilli-Armstrong (BCC)). (a) Shows simulation for Hoge and Mukherjees data (Table XII). (b) Shows simulation for Chen and Gray's data (Table XII). Note scale units are in cm.

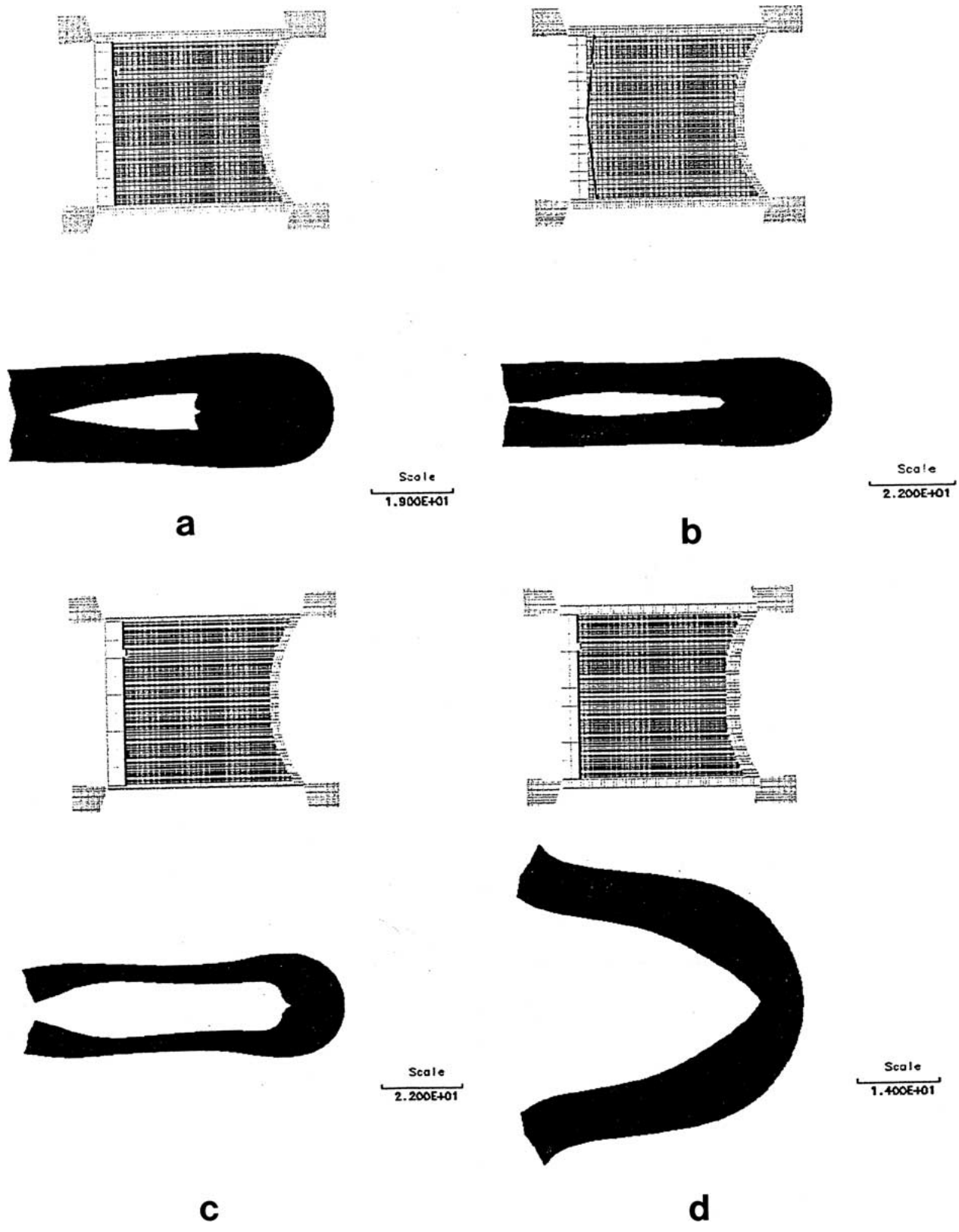

Figure 12 Effect of liner shape and thickness and case dimensions on the simulated EFP shape for iron. (a) Optimum simulation for reference. (b) EFP elongation due to 84° detonation angle with reference to axial, horizontal line through case center. (c) Elongated, hollow EFP resulting from change of case thickness from 2 mm in (a) to 5 mm. (d) Incomplete EFP resulting by changing the liner thickness from 5 mm in (a) to 8 mm. The corresponding dimensions are indicated by scale markers (in cm).

the detonation along a plane making an angle of approximately 84° to the horizontal (compared to a vertical plane of detonation as shown in Fig. 12a), the EFP stretches approximately 40% more. Blache and Weimann [6] found that such contoured detonation waves impart greater energy to the liner than point-initiated or plane waves. Fig. 12c shows the effect of a 2 mm thick case as opposed to a 5 mm thick case, as shown in Fig. 12a. It is seen that a lighter confinement produces a more elongated and hollow EFP compared to a heavier confinement. Bender and Carleone [8] also observed this effect. Increasing the liner

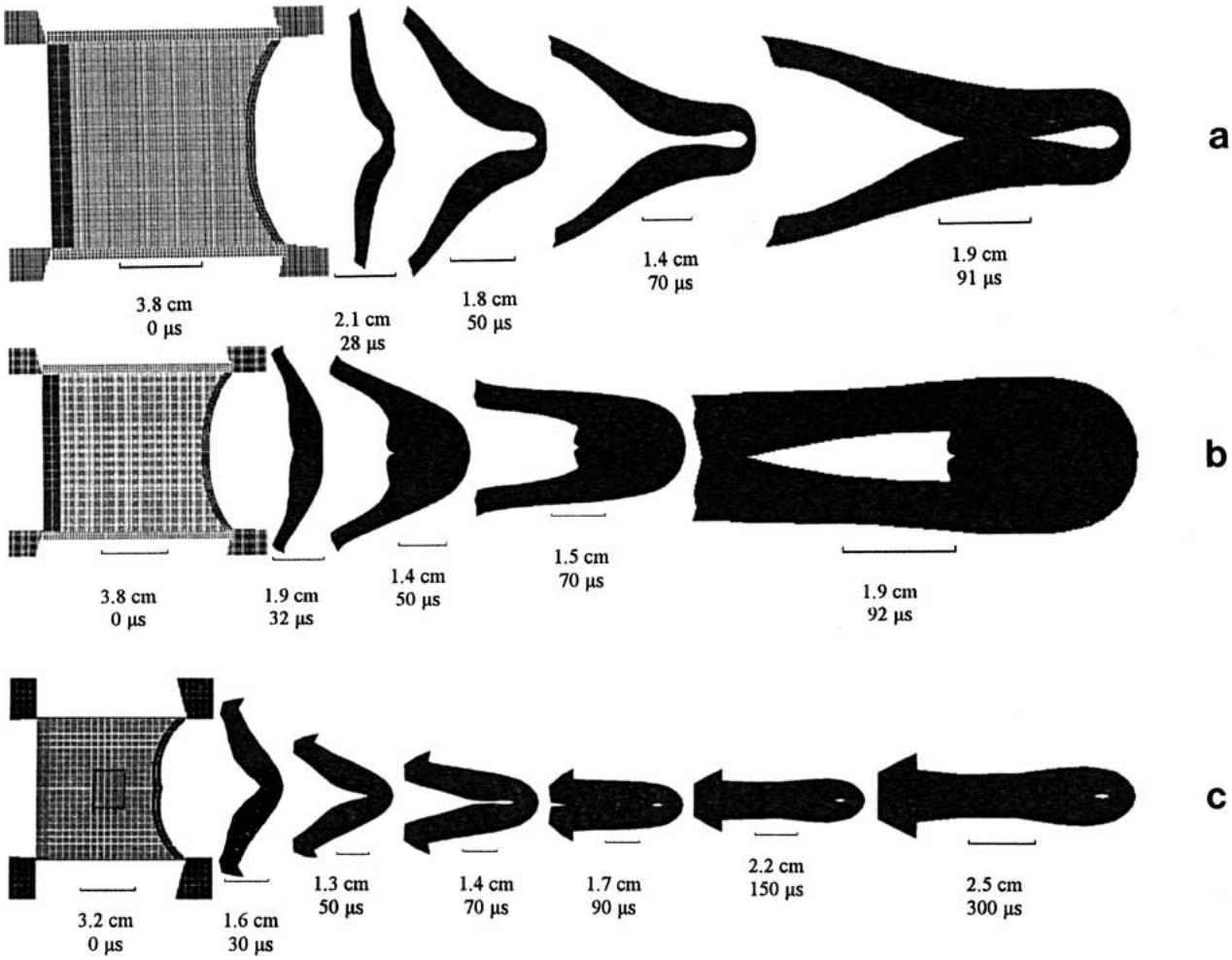

Figure 13 AUTODYN-2D simulations for stages of EFP formation utilizing the optimum, final simulations based on geometrical factors and microhardness-yield stress profile matching. (a) Ta; (b) Fe; (c) Cu. The zone within the case in (c) is a wave shaper (aluminum block) placed within the explosive. The dimensions at each stage shown are represented by appropriate markers.

TABLE XII Zerilli-Armstrong constitutive parameters from different sources

Parameter	Zerilli-Armstrong Constitutive Parameters from	
	Hoge and Mukherjee's data [38, 39]	Chen and Gray's data [40]
σ_0 (MPa)	30	140
C_1 (MPa)	1125	1750
C_3 (K^{-1})	0.00535	0.00975
C_4	0.000327	0.000675
C_5 (MPa)	310	650
n	0.44	0.65

thickness results in an EFP with a smaller length, which may not even fold back on itself if the liner is sufficiently thick, as shown in Fig. 12d. The liner thickness in this simulation was 8 mm as compared to 5 mm in Fig. 12a.

It was shown above that there are a number of factors affecting the final EFP shape and properties, and a validation that goes beyond matching shapes is a must in order to enable the codes to be used for designing these projectiles. Once such a validation is achieved, the simulation can be stopped at various stages of EFP formation as shown in Fig. 13, and the stress, strain and temperature profiles studied to explain the otherwise intractable microstructural evolution.

4. Conclusions

Ta, Fe and Cu have found wide acceptance in EFP applications because of their favorable properties. Although these three materials share a common platform in terms of their usefulness, they have significant differences that affect the mechanisms by which they (de)form. Whereas Ta and Fe have a BCC crystal structure, Cu has an FCC structure. They also possess widely differing melting temperatures. Ta melts at 3020°C, Fe at 1539°C and Cu at 1083°C. These differences are expected to affect the deformation behavior and the microstructural evolution in these materials. Under the high-strain, high-strain-rate deformation conditions, the interplay between the various hardening and softening mechanisms becomes even more complex. This complexity is very obvious from the fact that Ta and Fe, which have the same crystal structure and have similar yield strength values, strain rate sensitivities and elastic constants, behave very differently under the influence of these extreme conditions [28, 41–43]. Also, conventional theories that use dislocation generation and arrangements to accommodate strains cannot be invoked to explain the superplastic behavior of these materials in the shock regime.

Mathematical modeling of such complex phenomena is not a trivial task, but with quantum leaps in

computer hardware and software technologies in the last decade, hydrocodes are increasingly being relied upon to design these warheads. However, validations of these codes have been done only by matching the experimental geometries of the EFPs. Quinones [18] has performed geometry based and material property based validations on hypervelocity impact craters. A validation that includes material properties allows for a greater confidence in the predictive capabilities of the code, making it useful for design purposes. The codes can be improved by improving the constitutive equations that describe the material behavior in the shock regime. This requires a proper understanding of the deformation mechanisms operating under these conditions. A detailed microstructural analysis is a necessary step in achieving that understanding.

In this work, an attempt was made to relate experimental and theoretical aspects of the EFP formation process. A detailed microstructural analysis of Ta, Fe and Cu EFPs has shown that the mechanisms operating under high-strain, high-strain-rate conditions can be extremely complex. Whereas extensive DRV characterized the Ta EFP and extensive and complete DRX the Cu EFP, extensive twinning and related DRV and DRX characterized the Fe EFP. Both Fe and Cu EFPs showed shear banding. Zerilli-Armstrong model predictions were better for Ta, Johnson-Cook for Fe, and both models were equally good for Cu.

Constitutive equations describing such complex material behavior under these extreme conditions should incorporate the effects of these mechanisms. Unless that is done, each validation would only be another fit to a particular set of data and will sorely lack the predictive capability that is so important if one were to design these warheads solely on the basis of hydrocode predictions. This work is a significant contribution in exposing the inherent flaws of a simple, geometry-based validation, and shows the importance of complementing it with a property-based validation. Once validations are done utilizing constitutive equations that incorporate these mechanisms, simulations can be stopped at various stages of EFP formation to understand the otherwise intractable microstructural evolution by analyzing the various contour plots. In short, the detailed microstructural analysis and the importance of structure-property based validation provided in this work calls for a thorough constitutive model addressing these issues.

Acknowledgments

This research was supported in part by a Mr. and Mrs. MacIntosh Murchison Endowment at UTEP, a U.S. Department of Defense, Defense Logistics Agency, Defense National Stockpile Center Grant No. DN-009, and by the U.S. Army Armament Research, Development and Engineering Center (ARDEC), Picatinny Arsenal, NJ through contracts DAAA21-94-C-0059, DAAE30-97-M-0910, and DAAE30-99-M-0180 + MOD # P00001 to P00005. Our sincerest thanks are due to Dr. Chris Weickert, Defence Research Establishment Suffield, Medicine Hat, Alberta, Canada for graciously providing us with the iron and copper EFP samples. We also thank Mr. Bence Gerber and Dr. Chris Quan, Century Dynamics, Inc., San Ramon, CA for their help with the AUTODYN-2D hydrocode.

References

1. H. J. P. O'GRADY, C. J. HAYHURST and G. E. FAIRLIE, in South African Ballistics Symp., Stellenbosch, South Africa, Nov. 1996.
2. G. R. JOHNSON, *Trans. ASME: J. Appl. Mech.* **48** (1981) 30.
3. C. A. WEICKERT, Ph.D. dissertation, Drexel University, Philadelphia, PA, June 1986.
4. J. O. HALLQUIST, User's Manual for DYNA2D—An Explicit Two-Dimensional Hydrodynamic Finite Element Code with Interactive Rezoning, Report UCID-18756, Lawrence Livermore National Laboratory, 1980.
5. G. RANDERS-PEHRSON, J. W. HERMANN, JR. and E. R. BERUS, in Proc. of the 3rd Intl. Symp. on Ballistics, Karlsruhe, Germany, March 23–25, 1977, p. F2 1.
6. A. BLACHE and K. WEIMANN, in Proc. of the 16th Intl. Symp. on Ballistics (American Defense Preparedness Association, 1996) Vol. 2: Exterior Ballistics, Warhead Mechanism, p. 337.
7. K. WEIMANN, *J. Propellants, Explosives, Pyrotechnics* **18** (1993) 294.
8. D. BENDER and J. CARLEONE, in "Tactical Missile Warheads," edited by J. Carleone, Progress in Astronautics and Aeronautics, Vol. 155 (American Institute of Aeronautics and Astronautics, Washington, DC, 1993).
9. S. K. YIU, in Proc. of the Eighth Intl. Symp. on Ballistics, Orlando, FL, 1984, p. VI-41.
10. J. L. M. J. VAN BREE, W. DUVALOIS and P. SOMOGY, in Proc. of the 16th Intl. Symp. on Ballistics (American Defense Preparedness Association, 1996) Vol. 2: Exterior Ballistics, Warhead Mechanism, p. 575.
11. K. WEIMANN *et al.*, in Proc. of the 12th Intl. Symp. on Ballistics, San Antonio, TX, Oct. 1990.
12. C. A. WEICKERT and P. J. GALLAGHER, in 16th Intl. Symp. on Ballistics, San Francisco, CA, Sept. 23–28, 1996.
13. *Idem.*, in Proc. of the 13th Intl. Symp. on Ballistics, Stockholm, Sweden, June 1992.
14. E. C. FACCINI and H. A. WOODBURY, *J. of Testing and Evaluation* **24**(2) (1996) 123.
15. A. M. S. HAMOUDA and M. S. J. HASHMI, *J. Mater. Proc. Tech.* **56** (1996) 847.
16. S. PAPPU and L. E. MURR, in Shock Compression of Condensed Matter-1999 (CP505), edited by M. D. Furnish, L. C. Chhabildas and R. S. Hixson (American Institute of Physics, Melville, NY, 2000) p. 1141.
17. *Idem.*, in Fundamental Issues and Applications of Shock-Wave and High-Strain-Rate Phenomena, Proceedings of EXPLOMET 2000, edited by K. P. Staudhammer, L. E. Murr and M. A. Meyers, to be published.
18. S. QUIÑONES, Ph.D. dissertation, The University of Texas at El Paso, El Paso TX, December 1996.
19. F. I. GRACE, in "Metallurgical and Materials Applications of Shock-Wave and High-Strain-Rate Phenomena," edited by L. E. Murr, K. P. Staudhammer and M. A. Meyers (Elsevier Science B. V., Amsterdam, The Netherlands, 1995) p. 521.
20. C. E. ANDERSON, JR., *Intl. J. of Impact Eng.* **5** (1987) 33.
21. F. J. ZERILLI and R. W. ARMSTRONG, *J. Appl. Phys.* **61**(5) (1987) 1816.
22. M. J. MURPHY, *J. de Physique IV, Colloque C8, supplément au J. de Physique III* **4** (1994) 483.
23. R. W. ARMSTRONG and F. J. ZERILLI, in "Advances in Twinning," edited by S. Ankem and C. S. Pande (The Minerals, Metals, and Materials Society, Warrendale, PA, 1999) p. 67.
24. *Idem.*, in "Fundamental Issues and Applications of Shock-Wave and High-Strain-Rate Phenomena," Proc. of EXPLOMET 2000, edited by K. P. Staudhammer, L. E. Murr and M. A. Meyers (Elsevier Science Publishers, 2000) in press.
25. U. R. ANDRADE, M. A. MEYERS and A. H. CHOKSHI, *Scripta Metall. et. Mater.* **30**(7) (1994) 933.
26. M. J. MURPHY and D. H. LASSILA, *J. de Physique IV, Colloque C3, supplément au J. de Physique III* **7** (1997) 655.

27. M. J. WORSWICK, N. QIANG, P. NIESSEN and R. J. PICK, in "Shock-Wave and High-Strain-Rate Phenomena in Materials," edited by M. A. Meyers, L. E. Murr and K. P. Staudhammer (Marcel-Dekker, Inc., NY, 1992) p. 87.
28. N. QIANG, P. NIESSEN and R. J. PICK, *Mater. Sci. Eng.* **A160** (1993) 49.
29. N-Y. TANG, P. NIESSEN, R. J. PICK and M. J. WORSWICK, *ibid.* **A131** (1991) 153.
30. C-S. NIOU, L. E. MURR, C. FENG and S. PAPPU, *Microstructural Science* **22** (1995) 73.
31. S. PAPPU, C-S. NIOU, C. KENNEDY and L. E. MURR, *ibid.* **23** (1996) 259.
32. L. E. MURR, C-S. NIOU and C. FENG, *Scripta Metall. Mater.* **31**(3) (1994) 297.
33. C. FENG, L. E. MURR and C-S. NIOU, *Metall. and Mater. Trans.* **27A** (1996) 1773.
34. L. E. MURR, S. PAPPU, C. KENNEDY, C-S. NIOU and M. A. MEYERS, in "Tantalum," edited by E. Chen, A. Crowson, E. Lavernia, W. Ebihara and P. Kumar (TMS, Warrendale, PA, 1996) p. 145.
35. M. J. WORSWICK, P. PELLETIER, J. FOWLER, P. J. GALLAGHER and C. A. WEICKERT, in "Metallurgical and Materials Applications of Shock-Wave and High-Strain-Rate Phenomena," edited by L. E. Murr, K. P. Staudhammer and M. A. Meyers (Elsevier Science B. V., Amsterdam, The Netherlands, 1995) p. 227.
36. S. PAPPU and L. E. MURR, *Mater. Sci. Eng. A* **284**(1/2) (2000) 148.
37. S. PAPPU, S. SEN, L. E. MURR, D. KAPOOR and L. S. MAGNESS, *ibid.* in press.
38. F. J. ZERILLI and R. W. ARMSTRONG, *J. Appl. Phys.* **68** (1990) 1580.
39. K. G. HOGE and A. K. MUKHERJEE, *J. Mater. Sci.* **12** (1977) 1666.
40. S. R. CHEN and G. T. GRAY III, *Metall. Mater. Trans.* **27A** (1996) 2994.
41. G. T. GRAY III and K. S. VECCHIO, *ibid.* **26A** (1995) 2555.
42. J. C. HUANG and G. T. GRAY III, *Mater. Sci. Eng. A* **103** (1988) 241.
43. G. E. DIETER, in "Response of Metals to High Velocity Deformation," edited by P. G. Shewmon and V. F. Zackay, Metallurgical Society Conference Proceedings, Vol. 9 (Interscience, New York, 1961) p. 409.

Received 17 April
and accepted 28 August 2001